Interference Analysis and Mitigation for Aerial IoT Considering 3D Antenna Patterns

Sung Joon Maeng, Mrugen A. Deshmukh, İsmail Güvenç, *Fellow, IEEE*, Arupjyoti Bhuyan, *Senior Member, IEEE*, and Huaiyu Dai, *Fellow, IEEE*

***Abstract*—Due to dense deployments of Internet of things (IoT) networks, interference management becomes a critical challenge. With the proliferation of aerial IoT devices, such as unmanned aerial vehicles (UAVs), interference characteristics in 3D environments will be different than those in the existing terrestrial IoT networks. In this paper, we consider 3D topology IoT networks with a mixture of aerial and terrestrial links, with low-cost cross-dipole antennas at ground nodes and both omni-directional and cross-dipole antennas at aerial nodes. Considering a massive-access communication scenario, we first derive the statistics of the channel gain at IoT receivers in closed form while taking into account the radiation patterns of both ground and aerial nodes. These are then used to calculate the ergodic achievable rate as a function of the height of the aerial receiver and the cumulative interference. We propose a low-complexity interference mitigation scheme that utilizes 3D antenna radiation pattern with different dipole antenna settings. Our results show that using the proposed scheme, the ergodic achievable rate improves as the height of the aerial receivers increases. In addition, we also show that the ratio between the ground and aerial receivers that maximizes the peak rate increases with the height of the aerial IoT receiver.**

***Index Terms*—5G, 3D topology, antenna radiation pattern, IoT, UAV, uncoordinated network.**

I. Introduction

With the emergence of 5G wireless networks and continuously increasing data demand from users, network densification becomes crucial to improve data throughput across various different 5G use cases [2]. In the prospective networks, various types of Internet of things (IoT) devices, such as sensors, mobile phones, vehicles, are pervasively present and connected together. Massive access IoT is thereby the growing concept where ubiquitous devices communicate and interact with each other [3]–[5]. In order to satisfy the growing demand for IoT devices, various different technologies have been developed and standardized. In particular, 3GPP developed the narrowband IoT (NB-IoT) specifications [6], [7], while LoRa and Sigfox are introduced as alternative low-power wide-area network (LPWAN) technologies [8].

Future IoT deployments are expected to involve various different kinds of devices and applications. Among them, communication with aerial devices, such as cellular-connected unmanned aerial vehicles (UAVs), has recently received major attention [9], [10]. UAVs have been considered as part of a 3D IoT network in [11] for crowd surveillance purposes, while 3D scenarios for IoT deployments have been considered in [12], [13] for RFID-based localization, and [14] provides a broader overview with 3D IoT deployments. The 3D communication, propagation, and interference scenarios for such low-complexity IoT networks introduce new challenges that need to be tackled for their effective deployment. In particular, with massive deployments of low-complexity IoT networks, interference management becomes a critical challenge [15], [16], which to our best knowledge has not been explored in detail in the 3D space.

The effect of 3D radiation pattern has been studied for massive MIMO beamforming in the literature, where angle dependent antenna gain incorporated with beamforming gain is studied [17]–[21]. 3D beamforming with UAVs have been explored in [22], [23], which considers the effect of the 3D antenna radiation pattern combined with the 3D spatial beamforming. However, these approaches, and associated interference mitigation schemes such as zero-forcing precoding, interference cancellation, and interference alignment may not be suitable for tackling with interference problems in 3D space for low-cost and low-complexity IoT devices. Such IoT devices typically operate below 1 GHz, and may employ only a single (or few) dipole antennas, and have limited computational capabilities. While dipole antenna radiation pattern with different configurations in the 3D space have been studied in [1], [24]–[26], there is no detailed analysis of interference characteristics and mitigation schemes with aerial equipment to our best knowledge.

In this paper, considering both aerial and ground IoT nodes, we derive the ergodic achievable rate in a 3D IoT network as a function of the height of UAVs, 3D antenna radiation patterns, and the cumulative interference statistics from all IoT transmitters. Subsequently, we propose a new interference mitigation scheme in uncoordinated IoT networks that utilizes the 3D radiation pattern of the dipole antenna. The main concept of our proposed interference mitigation scheme is that if we utilize

Manuscript received June 8, 2020; revised October 26, 2020; accepted December 3, 2020. Date of publication December 21, 2020; date of current version February 12, 2021. This work was supported in part by INL Laboratory Directed Research Development (LDRD) Program under DOE Idaho Operations Office Contract DEAC07-05ID14517, and in part by NSF CNS through Award no. 1 814 727. The review of this article was coordinated by Dr. Chau Yuen. *(Corresponding author: Sung Joon Maeng.)*

Sung Joon Maeng, Mrugen A. Deshmukh, İsmail Güvenç, and Huaiyu Dai are with the Department of Electrical and Computer Engineering, North Carolina State University, Raleigh, NC 27 606 USA (e-mail: smaeng@ncsu.edu; madeshmu@ncsu.edu; iguvenc@ncsu.edu; hdai@ncsu.edu).

Arupjyoti Bhuyan is with INL Wireless Security Institue, Idaho National Laboratory, Idaho Falls, ID 83 402 USA (e-mail: arupjyoti.bhuyan@inl.gov).

Digital Object Identifier 10.1109/TVT.2020.3046121

the different antenna radiation pattern at the transmitter side depending on the 3D location of the receiver, we can suppress interference signal and enhance the desired signal. In general, in a 2D space topology we assume that the dipole antenna is aligned with z-axis, which generates omni-directional radiation pattern with respect to azimuth angle. However, this dipole setting, which may be common in typical low-cost IoT devices, cannot have onmi-directional radiation in 3D (as in networks including aerial nodes) due to power that varies with the elevation angle. On the other hand, by aligning dipole antenna with different direction, such as y-axis, we can obtain a different directivity of the radiation pattern.

In our previous work [1], we investigate the interference mitigation scheme by the 3D radiation pattern in the 3D topology network with similar setting. In particular, we propose 2 and 3 dipole antenna schemes in order to generate various radiation patterns depending on antenna configurations, and show the performance improvement by varying the height of the aerial devices and the proportion of the aerial devices by simulations. On the other hand, in this paper, different than [1], we focus on both analytically and numerically showing the performance improvement based on the concrete 3D topology channel model and solving the ergodic achievable rate. The contributions of the present paper can be listed as follows.

- We propose a 3D topology channel model based on the antenna patterns and the location of the devices. We introduce uniformly-distributed azimuth angle (ϕ) and distance in the 2D plane (r) in order to derive the distribution of the 3D distance between the IoT transmitters and receivers.
- Using the distribution of the distance and angles, we derive the closed-form equations of the expectation of the channel gains, which incorporates pathloss, small-scale fading, and antenna gain.
- We derive the ergodic achievable rate of the aerial receivers with different dipole antenna setting, and propose the cross-dipole antenna scheme that improves the rate compared with the conventional single dipole scheme.
- By numerical results, we show that the proposed cross-dipole scheme outperforms the single dipole scheme, and the ergodic achievable rate grows as the height of the aerial receiver increases. In addition, we show the best ratio between the ground receiver and aerial receiver with the different height of the aerial receivers.
- We introduce LoS / NLoS probability to model the pathloss, and we show that mixture LoS/NLoS pathloss model improves the ergodic sum rate at the low height range of aerial receivers when compared with the free-space pathloss model.

The rest of this paper is organized as follows. Section II provides the IoT system model with both ground and aerial IoT nodes. Section III analyzes the effect of 3D antenna radiation patterns on the IoT link qualities in a mixed air/ground IoT network considering both single-transmitter and multiple transmitter scenarios. Section IV derives the ergodic rates in such a multi-access IoT network, and proposes an antenna selection scheme for interference mitigation. Section V provides numerical results for an IoT network with mixed ground/aerial links, and the last section concludes the paper.

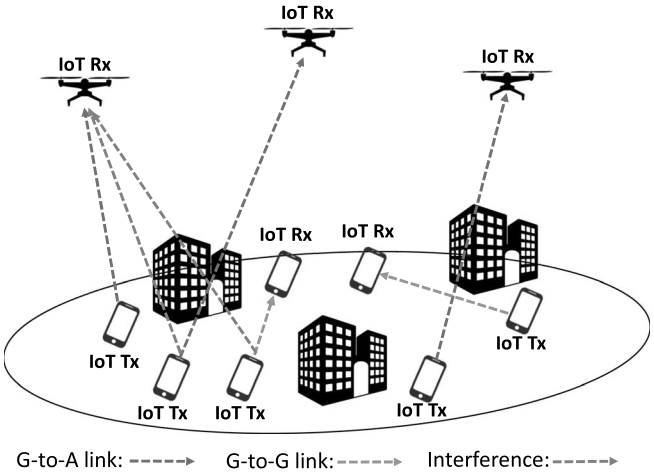

Fig. 1. Illustration of the 3D topology of the IoT network with both ground and aerial nodes.

Notation: $X \sim \mathcal{U}[a, b]$ denotes that the random variable X is uniformly distributed between a and b. $\mathcal{CN}(0, 1)$ defines a complex Gaussian distribution with mean zero and variance one. $\mathbb{E}\{X\}$ denotes the expectation of the random variable X.

II. System Model

In this study, we consider uncoordinated network with IoT devices as shown in Fig. 1. Transmitter and receiver pairs are distributed in 3D space without resource management from a central base station. Thus, time and frequency resources are shared by transmitter/receiver (Tx/Rx) pairs. IoT devices are divided into ground and aerial devices depending on the typical altitude of the device. For example, the sensor is regarded as a ground device, and the UAV is considered as an aerial device. We consider the case that all IoT Txs are ground devices, while IoT Rxs are either ground or aerial devices. Thus, there are simultaneous ground to ground (G-to-G) and ground to air (G-to-A) links in the same environment. Such communication topologies may be typical e.g., to support FAA remote-ID signaling for UAVs [27] with long-range IoT links, or simply for UAVs to collect sensory data from ground nodes, in the presence of other coexisting G-to-G IoT communications.

A. 3D Topology Based Channel Model

The channel between a transmitter and a receiver is modeled by pathloss, small-scale fading, and antenna gain. The distance between transmitter and receiver is easily derived by the 3D Cartesian coordination of two devices. Let $(x_i^{\mathrm{Tx}}, y_i^{\mathrm{Tx}}, z_i^{\mathrm{Tx}})$, $(x_i^{\mathrm{Rx}}, y_i^{\mathrm{Rx}}, z_i^{\mathrm{Rx}})$ denote the positions of Tx and Rx of i_{th} pair. Then, the distance between Tx and Rx is calculated as $d_{i,i} = \sqrt{(x_i^{\mathrm{Tx}} - x_i^{\mathrm{Rx}})^2 + (y_i^{\mathrm{Tx}} - y_i^{\mathrm{Rx}})^2 + (z_i^{\mathrm{Tx}} - z_i^{\mathrm{Rx}})^2}$. Then, the free-space pathloss can be expressed as

$$\beta_{i,i} = \left(\frac{4\pi d_{i,i}}{\lambda}\right)^2, \tag{1}$$

where λ is the wave length of the signal. We denote α as the small scale fading coefficient, and G_i^{Tx}, G_i^{Rx} are the antenna gains at the transmitter and the receiver sides, respectively. The

channel coefficient $g_{i,i}$ can be written by

$$g_{i,i} = \sqrt{PG_i^{\mathrm{Tx}}/(\beta_{i,i})G_i^{\mathrm{Rx}}}\alpha_{i,i}, \tag{2}$$

where P is signal power from the transmitter. The magnitude of small scale fading coefficient follows Rayleigh distribution, $\alpha \sim \mathcal{CN}(0,1)$. Although we consider NLoS small scale fading model due to long-distance IoT link, air-to-ground channels can be also modeled by Rician fading, in which the LoS component is dominant depending on the channel environment, as:

$$g_{i,i} = \sqrt{PG_i^{\mathrm{Tx}}/(\beta_{i,i})G_i^{\mathrm{Rx}}}\left\{\sqrt{\frac{\kappa}{\kappa+1}} + \sqrt{\frac{1}{\kappa+1}}\alpha_{i,i}\right\}, \tag{3}$$

where κ is the power ratio between the LoS and NLoS components. We consider Rician fading channel model by simulation results in Section V-F. The antenna gain G_i^{Tx}, G_i^{Rx} is the function of the angle of departure (AoD) and the angle of arrival (AoA). The angle can be represented by the azimuth angle (ϕ) and the elevation angle (θ), and the function G_i^{Tx}, G_i^{Rx} is changed depending on the antenna model.

B. Pathloss With LoS / NLoS Probability

The LoS probability for G-to-A links can be modeled by taking into account the blockages due to buildings. The International Telecommunication Union (ITU) suggests a probabilistic G-to-A LOS model for various different standard environments [28]. In particular, a simplified probabilistic LoS model is provided in [29] for UAVs, given by:

$$\mathbf{P}_{\mathrm{LoS}} = \frac{1}{1 + a_1 \exp\left(-a_2[90 - \frac{180\theta}{\pi} - a_1]\right)}, \tag{4}$$

where parameters a_1, a_2 are determined by the environment, and θ represents the elevation angle. The NLoS probability is $\mathbf{P}_{\mathrm{NLoS}} = 1 - \mathbf{P}_{\mathrm{LoS}}$. Then, the average pathloss in a given environment is calculated as

$$\beta_{\mathrm{avg}} = \mathbf{P}_{\mathrm{LoS}}(\eta_{\mathrm{LoS}}\beta) + \mathbf{P}_{\mathrm{NLoS}}(\eta_{\mathrm{NLoS}}\beta), \tag{5}$$

where η_{LoS} and η_{NLoS} denote the excessive pathloss of the LoS and the NLoS links, respectively, and β is the free-space pathloss as in (1). Note that $(\eta_{\mathrm{LoS}}, \eta_{\mathrm{NLoS}})$ [dB] for the 700 MHz carrier frequency is (0.6, 17) for urban and (1, 20) for dense urban environments, respectively [30].

Different pathloss models are compared in Fig. 2 as a function of aerial receiver height, considering the free-space path loss model in (1), as well as the mixture LoS/NLoS path loss model in (5) for urban and dense-urban environments. We observe that the free-space pathloss keeps increasing as the height of the device increases due to the larger link distance. However, for the mixture LoS/NLoS pathloss models, the pathloss decreases for the low-height regime while it increases after a critical height. This is due to the fact that the NLoS probability is high at the low height regime, and it keeps decreasing as the aerial receiver height increases. For larger receiver heights, the NLoS probability converges to zero, and hence the mixture LoS/NLoS pathloss becomes similar to the free-space model.

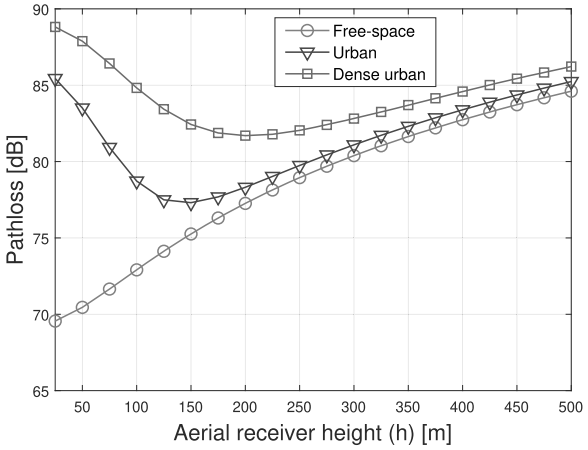

Fig. 2. Pathloss versus aerial receiver height for different pathloss models.

C. Ergodic Achievable Rate

The ergodic achievable rate of the aerial receiver can be represented by the channel gain from the connected transmitter, interference from other transmitters, and additive noise, as:

$$S_i = \mathbb{E}\left\{\log_2\left(1 + \frac{|g_{i,i}|^2}{\sum_{j\neq i}|g_{i,j}|^2 + \sigma_n^2}\right)\right\}, \tag{6}$$

where S_i is the ergodic achievable rate of the aerial receiver (i_{th} receiver), and σ_n^2 is the noise variance. We can approximate the ergodic achievable rate in (6) as

$$\begin{aligned} S_i &\overset{(a)}{\approx} \mathbb{E}\left\{\log_2\left(1 + \frac{|g_{i,i}|^2}{\sum_{j\neq i}|g_{i,j}|^2}\right)\right\} \\ &\overset{(b)}{\approx} \log_2\left(1 + \frac{\mathbb{E}\{|g_{i,i}|^2\}}{\sum_{j\neq i}\mathbb{E}\{|g_{i,j}|^2\}}\right), \end{aligned} \tag{7}$$

where (a) comes from the assumption that the effect of noise is trivial in the interference dominant network, and (b) comes from the approximation related with Jensen's inequality [31], [32]. Note that the approximation (b) holds if $|g_{i,i}|^2$, $|g_{i,j}|^2$ are non-negative, and it is more accurate as the number of random variables increase.

III. Effect of Antenna Radiation Pattern on 3D Topology Networks

In this section, we study the effect of 3D antenna radiation pattern in channel gain $|g_{i,i}|^2$ and achievable rate S. We assume that ground transmitters utilize cross-dipole antenna, and receivers utilize onmi-directional antenna. We take into account the cross-dipole antennas configuration, which deploys two dipole antenna on the orthogonal orientation. One is placed on the z-axis and the other is placed on the y-axis of Cartesian coordinate. We consider the transmitter structure that is able to select one of the two dipole antennas by external antenna network, either z-axis or y-axis. Thus, the ground transmitters are able to transmit the signal with either the z-axis dipole antenna or the y-axis dipole antenna. At first, we consider stand-alone

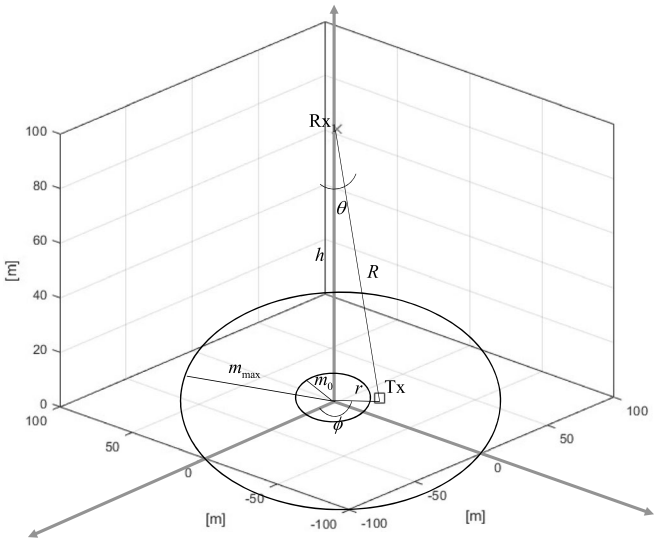

Fig. 3. 3D topology of IoT network in stand-alone scenario.

case, which means that only one Tx/Rx pair is located at a given space. Then, we expand it to multiple Tx/Rx scenario.

A. Analysis of Stand-Alone Scenario

1) PDF of Random Variables Related With the Location of Devices: Let consider one Tx/Rx pair. The location of ground transmitter is decided by the 2D circle radius (r) and azimuth angle (ϕ), and the location of aerial receiver is fixed at $(0, 0, h)$ Cartesian coordinate. The illustration of the 3D topology of the IoT network is shown in Fig. 3. The random variables r, ϕ are independently uniformly distributed as

$$f_r(r) = \frac{1}{m_{\max} - m_0},\ [m_0 < r < m_{\max}],$$
$$f_\phi(\phi) = \frac{1}{2\pi},\ [0 < \phi < 2\pi], \tag{8}$$

where $f_r(r)$, $f_\phi(\phi)$ are the probability density function (PDF) of r and ϕ, while m_0, $m_{\max}$ are the minimum and the maximum radius of the circle, respectively. The elevation angle (θ) can be represented as $\theta = \tan^{-1}(\frac{r}{h})$. Then, the PDF of random variable θ can be derived by

$$\begin{aligned} \mathrm{d}\theta &= \frac{h}{r^2 + h^2}\mathrm{d}r, \\ f_\theta(\theta) &\overset{(a)}{=} \sum f_r(h\tan\theta)\left|\frac{\mathrm{d}r}{\mathrm{d}\theta}\right| \\ &= \sum f_r(h\tan\theta)\left|\frac{h^2\tan^2\theta + h^2}{h}\right| \\ &= \sum f_r(h\tan\theta)(h\tan^2\theta + h) \\ &= \frac{h}{(m_{\max} - m_0)}\tan^2\theta + \frac{h}{(m_{\max} - m_0)}, \\ &\left[\tan^{-1}\left(\frac{m_0}{h}\right) < \theta < \tan^{-1}\left(\frac{m_{\max}}{h}\right)\right], \end{aligned} \tag{9}$$

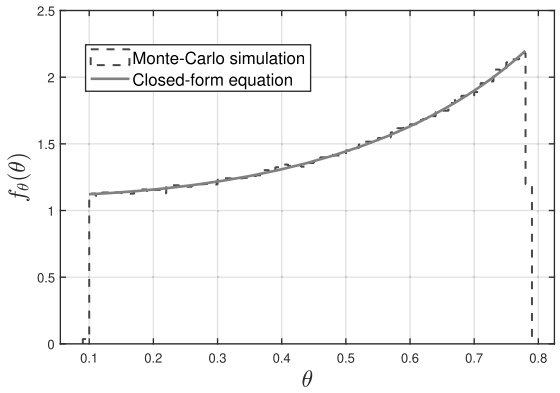

Fig. 4. PDF of random variable θ on stand-alone scenario in (9). $m_0 = 10$, $m_{\max} = 100$, $h = 100$.

where (a) comes from the PDF transformation function. The distance between Tx and Rx is easily obtained as $R = \frac{h}{\cos\theta}$. The PDF of θ in (9) is shown in Fig. 4, which is confirmed by Monte-Carlo simulation.

2) Antenna Radiation Pattern of Cross-Dipole Antenna: The radiation pattern of dipole antenna is interpreted by normalized antenna field pattern F. If we place the dipole antenna on z-axis, the radiation pattern is onmi-directional to azimuth angle (ϕ). The normalized antenna field pattern of z-axis dipole antenna is written as [33], [34]:

$$F_{\mathrm{z}}(\theta) = \frac{\cos\left(\frac{\pi f_0 d_{\mathrm{len}}}{c}\cos\theta\right) - \cos\left(\frac{\pi f_0 d_{\mathrm{len}}}{c}\right)}{\sin\theta}, \tag{10}$$

where d_{len}, c, f_0 denote the length of dipole antenna, the speed of light, and the carrier frequency, respectively. If we assume half-wave length dipole antenna ($d_{\mathrm{len}} = \frac{\lambda}{2}$), $\frac{\pi f_0 d_{\mathrm{len}}}{c} = \frac{\pi}{2}$ holds. Then, (10) can be rewritten as

$$F_{\mathrm{z}}(\theta) = \frac{\cos\left(\frac{\pi}{2}\cos\theta\right)}{\sin\theta}. \tag{11}$$

Let dipole antenna be placed on y-axis. The angle between the dipole antenna direction and the signal propagation direction is $\cos^{-1}(\hat{\mathbf{s}}\cdot\hat{\mathbf{y}}) = \cos^{-1}(\sin(\theta)\sin(\phi))$, where $\hat{\mathbf{s}}$, $\hat{\mathbf{y}}$ are the unit vector of the signal and y-axis. Then, the normalized antenna field pattern of y-axis dipole antenna is given by

$$F_{\mathrm{y}}(\theta,\phi) = \frac{\cos\left(\frac{\pi}{2}\cos\left(\cos^{-1}(\sin(\theta)\sin(\phi))\right)\right)}{\sin\left(\cos^{-1}(\sin(\theta)\sin(\phi))\right)}. \tag{12}$$

Note that the antenna field pattern of y-axis is the function of both the azimuth angle (ϕ) and the elevation angle (θ). It means that the antenna gain can be changed by varying the azimuth angle as well as the elevation angle. Normalizedfield patterns of the z-axis and the y-axis dipole antenna from (11) and (12), respectively, are shown in Fig. 5 on the Cartesian coordinates.

3) The Expectation of the Channel Gain: The statistical knowledge of the channel gain is important in order to obtain the achievable rate of the user or system. We hence derive the expectation of the channel gain $\mathbb{E}\{|g_{i,i}|^2\}$ here, to calculate the ergodic achievable rate later on. If we consider a z-axis dipole antenna on the ground transmitter ($G_i^{\mathrm{Tx}} = F_{\mathrm{z}}^2$) and an

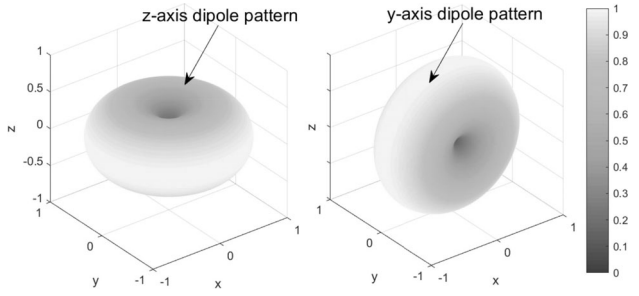

Fig. 5. Field pattern of dipole antenna on Cartesian coordinate (normalized magnitude).

omni-directional antenna on the aerial receiver ($G_i^{\mathrm{Rx}} = 1$), we can express the expectation of the channel gain from (1), (2) as follows:

$$\begin{aligned}\mathbb{E}\{|g_{i,i}|^2\}_{\mathrm{z}} &= \mathbb{E}\{PF_{\mathrm{z}}^2/(\beta)\alpha^2\} \\ &\overset{(a)}{=} \frac{P\lambda^2}{16\pi^2}\mathbb{E}\left\{\alpha^2\right\}\mathbb{E}\left\{\frac{(F_{\mathrm{z}})^2}{R^2}\right\} \\ &\overset{(b)}{=} k_1\mathbb{E}\left\{\frac{(F_{\mathrm{z}})^2}{R^2}\right\}. \end{aligned} \tag{13}$$

Since α is independent of the positions of devices, (a) holds, and (b) comes from $k_1 = \frac{P\lambda^2}{16\pi^2}$, $\mathbb{E}\{\alpha^2\} = 1$. By using (11), (13) can be rewritten as

$$\begin{aligned}&\mathbb{E}\{|g_{i,i}|^2\}_{\mathrm{z}} \\ &= k_1\mathbb{E}\left\{\left(\frac{\cos\left(\frac{\pi}{2}\cos\theta\right)}{\sin\theta}\right)^2\frac{\cos^2\theta}{h^2}\right\} \\ &\overset{(a)}{=} k_1\int\left(\frac{\cos\left(\frac{\pi}{2}\cos\theta\right)}{h\sin\theta}\right)^2\cos^2\theta\; f_\theta(\theta)\mathrm{d}\theta \\ &\overset{(b)}{=} \frac{k_1}{(m_{\max}-m_0)h}\int_{\tan^{-1}\left(\frac{m_0}{h}\right)}^{\tan^{-1}\left(\frac{m_{\max}}{h}\right)}\left(\frac{\cos\left(\frac{\pi}{2}\cos\theta\right)}{\sin\theta}\right)^2 \\ &\quad\times\cos^2\theta\,(1+\tan^2(\theta))\mathrm{d}\theta \\ &\overset{(c)}{=} \frac{k_1}{(m_{\max}-m_0)h}\int_{\tan^{-1}\left(\frac{m_0}{h}\right)}^{\tan^{-1}\left(\frac{m_{\max}}{h}\right)}\left(\frac{\cos\left(\frac{\pi}{2}\cos\theta\right)}{\sin\theta}\right)^2\mathrm{d}\theta, \end{aligned} \tag{14}$$

where (a) comes from the definition of the expectation, (b) comes from (9), and (c) comes from $1+\tan^2(\theta) = \sec^2(\theta)$. Since there is no closed-form equation for (14), we utilize asymptotic behavior to approximate the equation. If the height of the aerial receiver (h) goes to infinity, the interval of the integral with respect to θ go to 0; $\tan^{-1}(\frac{m_{\max}}{h}) \to 0,\ \text{as } h \to \infty$. Then, we can apply Taylor series approximation at $\theta = 0$, to obtain:

$$\begin{aligned}&\mathbb{E}\{|g_{i,i}|^2\}_{\mathrm{z}} \\ &\approx \frac{k_1}{(m_{\max}-m_0)h}\int_{\tan^{-1}\left(\frac{m_0}{h}\right)}^{\tan^{-1}\left(\frac{m_{\max}}{h}\right)}\left(\frac{\pi^2\theta^2}{16}\right)\mathrm{d}\theta, \\ &= \frac{\pi^2 k_1\left[\left\{\tan^{-1}\left(\frac{m_{\max}}{h}\right)\right\}^3-\left\{\tan^{-1}\left(\frac{m_0}{h}\right)\right\}^3\right]}{48(m_{\max}-m_0)h}, \end{aligned} \tag{15}$$

where $(\frac{\pi^2\theta^2}{16})$ is the first term of Taylor series.

Now, if we consider y-axis dipole antenna for the ground transmitter, we can derive the channel gain by similar way:

$$\begin{aligned}&\mathbb{E}\{|g_{i,i}|^2\}_{\mathrm{y}} \\ &= k_1\mathbb{E}\left\{\frac{(F_{\mathrm{y}})^2}{R^2}\right\} \\ &\overset{(a)}{=} k_1\int\int\left(\frac{\cos\left(\frac{\pi}{2}\cos(\cos^{-1}(\sin(\theta)\sin(\phi)))\right)}{h\sin\left(\cos^{-1}(\sin(\theta)\sin(\phi))\right)}\right)^2 \\ &\quad\times\cos^2\theta\; f_\theta(\theta)f_\phi(\phi)\mathrm{d}\theta\mathrm{d}\phi \\ &\overset{(b)}{=} \frac{k_1}{2\pi h(m_{\max}-m_0)}\int_0^{2\pi}\int_{\tan^{-1}\left(\frac{m_0}{h}\right)}^{\tan^{-1}\left(\frac{m_{\max}}{h}\right)} \\ &\quad\times\left(\frac{\cos\left(\frac{\pi}{2}\cos(\cos^{-1}(\sin(\theta)\sin(\phi)))\right)}{\sin\left(\cos^{-1}(\sin(\theta)\sin(\phi))\right)}\right)^2\mathrm{d}\theta\mathrm{d}\phi, \end{aligned} \tag{16}$$

where (a) comes from the definition of the expectation and (12), and (b) comes from the PDF functions in (8). In the similar manner, since there is no closed-form equation for (16), if the height (h) goes to infinity, we can apply Taylor series approximation at $\theta = 0$, to obtain:

$$\begin{aligned}&\mathbb{E}\{|g_{i,i}|^2\}_{\mathrm{y}} \\ &\approx \frac{k_1}{2\pi h(m_{\max}-m_0)}\int_0^{2\pi}\int_{\tan^{-1}\left(\frac{m_0}{h}\right)}^{\tan^{-1}\left(\frac{m_{\max}}{h}\right)} \\ &\quad\times\left(1-\frac{1}{4}(\pi^2-4)\sin^2(\phi)\theta^2\right)\mathrm{d}\theta d\phi \\ &= \frac{k_1}{2\pi h(m_{\max}-m_0)}\int_0^{2\pi} \\ &\times\left(\frac{(4-\pi^2)\sin^2(\phi)\left[\left\{\tan^{-1}\left(\frac{m_{\max}}{h}\right)\right\}^3-\left\{\tan^{-1}\left(\frac{m_0}{h}\right)\right\}^3\right]}{12}\right. \\ &\quad\left.+\tan^{-1}\left(\frac{m_{\max}}{h}\right)-\tan^{-1}\left(\frac{m_0}{h}\right)\right)\mathrm{d}\phi \\ &= \frac{k_1}{2\pi h(m_{\max}-m_0)} \\ &\quad\times\left(\frac{(4\pi-\pi^3)\left[\left\{\tan^{-1}\left(\frac{m_{\max}}{h}\right)\right\}^3-\left\{\tan^{-1}\left(\frac{m_0}{h}\right)\right\}^3\right]}{12}\right. \\ &\quad\left.+2\pi\tan^{-1}\left(\frac{m_{\max}}{h}\right)-2\pi\tan^{-1}\left(\frac{m_0}{h}\right)\right), \end{aligned} \tag{17}$$

where $(1-\frac{1}{4}(\pi^2-4)\sin^2(\phi)\theta^2)$ is the first and the second terms of Taylor series at $\theta = 0$ with fixed ϕ. The tightness of the approximated close-form equations (15), (17) is shown by simulation in Fig. 6. It is observed that (15) is really close to the exact value even if the height (h) is low, and (17) becomes close to the exact value as h increases. Note that the approximations should be more accurate at higher height, since we use $h \to \infty$.

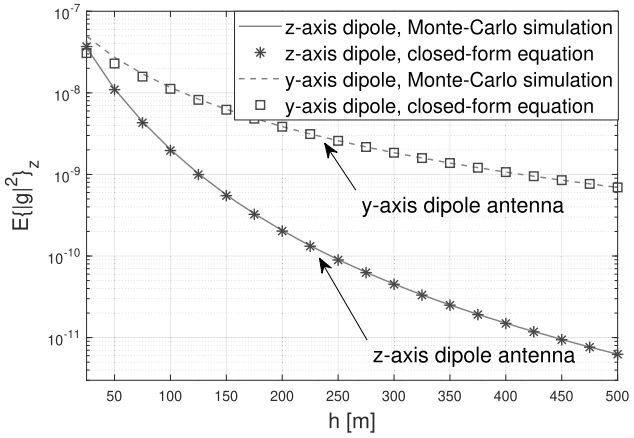

Fig. 6. Expectation of the channel gain versus height (h) with different dipole antenna placement on stand-alone scenario in (15), (17), and $m_0 = 10$, $m_{\max} = 100$.

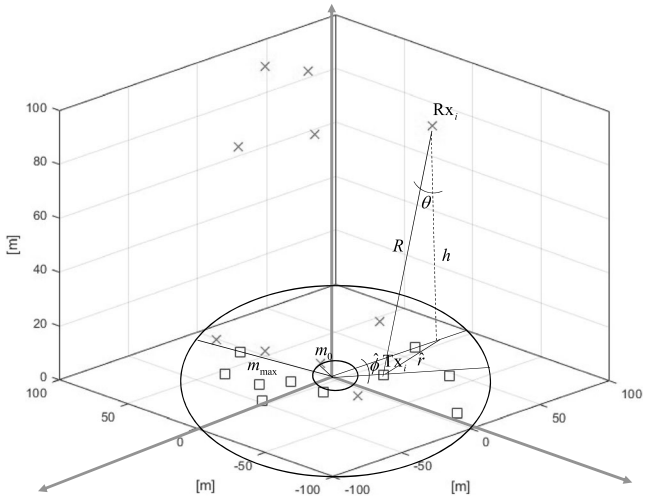

Fig. 7. 3D topology design in IoT network on multiple Tx/Rx pairs scenario.

B. Analysis of Multiple Tx Scenario

Let us consider multiple transmitters on the ground, and an aerial receiver is fixed at $(0, 0, h)$ Cartesian coordinate. Let us assume that one ground transmitter which is connected with the aerial receiver utilizes either z-axis dipole antenna or y-axis dipole antenna, and all other ground transmitters select z-axis dipole antenna. We compare the achievable rate S of the aerial receiver depending on the dipole antenna selection from the connected ground transmitter. As mentioned before, ground transmitters have cross-dipole antenna and they are capable of selecting either z-axis or y-axis dipole antenna. Intuitively, we can observe from the antenna field patterns that z-axis dipole achieves higher antenna gain to ground receivers, and y-axis dipole antenna obtains better performance to aerial receivers.

Let consider the case that the ground transmitter connected with the aerial receiever utilizes z-dipole antenna. Then, $\mathbb{E}\{|g_{i,i}|^2\}$ is equal to $\mathbb{E}\{|g_{i,i}|^2\}_{\mathrm{z}}$ in (15). Since other transmitters utilize z-dipole antenna, $\mathbb{E}\{|g_{i,j}|^2\}$ is also equal to $\mathbb{E}\{|g_{i,i}|^2\}_{\mathrm{z}}$. If we assume that the number of pairs of Tx/Rx is K and substitute $\mathbb{E}\{|g_{i,i}|^2\}_{\mathrm{z}}$ in (15) for ζ_{z}, the ergodic achievable rate of the aerial receiver from (7) can be written as

$$\{S_i\}_{\mathrm{z}} \approx \log_2\left(1 + \frac{\zeta_z}{(K-1)\zeta_z}\right) = \log_2\left(1 + \frac{1}{(K-1)}\right). \tag{18}$$

Note that the ergodic achievable rate with z-dipole antenna is only depending on the number of pairs (K) in the network. The reason for this is that either desired signal or interference signal has the same statistical values.

Next, let us consider the case that the ground transmitter utilizes y-dipole antenna. At this time, the channel gain from the desired signal $\mathbb{E}\{|g_{i,i}|^2\}$ is equal to $\mathbb{E}\{|g|^2\}_{\mathrm{y}}$ in (17). Then, after we substitute $\mathbb{E}\{|g|^2\}_{\mathrm{y}}$ for ζ_{y}, the ergodic achievable rate of the aerial receiver can be expressed as

$$\{S_i\}_{\mathrm{y}} \approx \log_2\left(1 + \frac{\zeta_{\mathrm{y}}(h)}{(K-1)\zeta_{\mathrm{z}}(h)}\right), \tag{19}$$

where channel gains $\zeta_{\mathrm{y}}(h), \zeta_{\mathrm{z}}(h)$ are the function of the height (h). We interestingly observe that the ergodic achievable rate from (19) improves as the height increases, while the ergodic achievable rate from (18) keeps constant as a function of the height, which is shown by simulations in Section V. It means that we can improve the performance of the achievable rate by utilizing different antenna radiation pattern depending on the type of the devices. For example, we can set the ground transmitters which are connected with the ground receiver to choose z-axis dipole antenna, and transmitters which are connected with the aerial receiver to select y-axis dipole antenna. Besides, we can obtain better performance, as the height of the aerial receiver is higher.

IV. Analysis of Multiple Tx/Rx Pairs Scenario

In this section, we extend the scenario to multiple Tx/Rx pairs without the limitation of the receivers' positions. It means that the receivers are not fixed at $(0, 0, h)$ Cartesian coordinate, but decided by random variables. Moreover, receivers could be either ground receiver or aerial receiver. We assume that the height of all aerial receivers is fixed to h. Fig. 7 shows the new illustration of 3D topology design in IoT network with multiple Tx/Rx pairs scenario.

A. PDF of Random Variables Related With Node Locations

At first, the location of the individual transmitters and receivers are decided by independently generated random variables. The PDF of uniformly distributed random variables that indicates the position of the devices are given by

$$\begin{aligned}
f_{r^{\mathrm{Tx}}}(r^{\mathrm{Tx}}) &= \frac{1}{m_{\max} - m_0},\ [m_0 < r^{\mathrm{Tx}} < m_{\max}],\\
f_{r^{\mathrm{Rx}}}(r^{\mathrm{Rx}}) &= \frac{1}{m_{\max} - m_0},\ [m_0 < r^{\mathrm{Rx}} < m_{\max}],\\
f_{\phi^{\mathrm{Tx}}}(\phi^{\mathrm{Tx}}) &= \frac{1}{2\pi},\ [0 < \phi^{\mathrm{Tx}} < 2\pi],\\
f_{\phi^{\mathrm{Rx}}}(\phi^{\mathrm{Rx}}) &= \frac{1}{2\pi},\ [0 < \phi^{\mathrm{Rx}} < 2\pi],
\end{aligned} \tag{20}$$

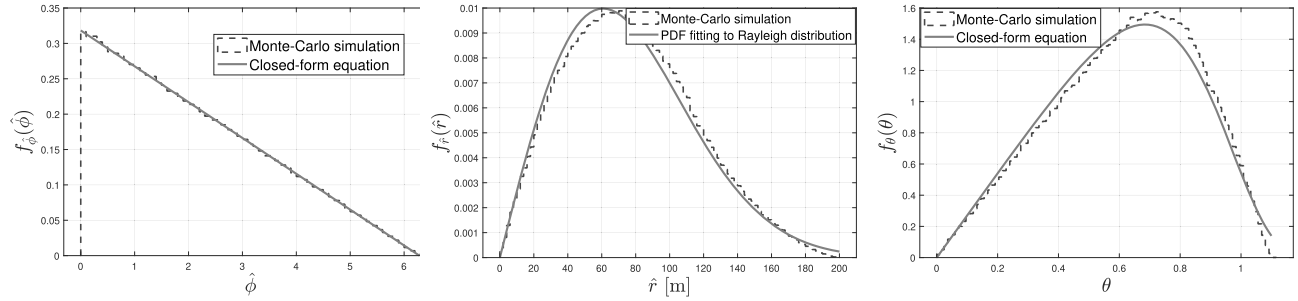

Fig. 8. PDF of random variables on multiple Tx/Rx scenario in (22), (23), (24), where $m_0 = 10$, $m_{\max} = 100$, $h = 100$. (a) The PDF of $\hat{\phi}$. (b) The PDF of $\hat{r}$. (c) The PDF of θ.

where r^{Tx}, r^{Rx} are the 2D circle radius of transmitters and receivers, and ϕ^{Tx}, ϕ^{Rx} are azimuth angle of transmitters and receivers. Since the location of both transmitters and receivers are determined by random variables, we need to calculate the relative difference of the Tx/Rx random variables in order to derive the distance between transmitters and receivers (R):

$$\hat{\phi} = |\phi^{\mathrm{Rx}} - \phi^{\mathrm{Tx}}|,$$
$$\hat{r} = \sqrt{(r^{\mathrm{Tx}})^2 + (r^{\mathrm{Rx}})^2 - 2r^{\mathrm{Tx}}r^{\mathrm{Rx}}\cos\hat{\phi}}, \tag{21}$$

where $\hat{\phi}$ is relative difference of azimuth angle between Tx and Rx, $\hat{r}$ is distance between Tx and Rx at 2D ground plane. The equation of $\hat{r}$ comes from the law of cosines in trigonometry. The PDF of $\hat{\phi}$ can be expressed as

$$f_{\hat{\phi}}(\hat{\phi}) = \frac{1}{2\pi^2}(2\pi - \hat{\phi}),\ [0 < \hat{\phi} < 2\pi], \tag{22}$$

where (22) is derived from the property that the PDF of the sum of the two independent random variables is the convolution of the PDF of two random variables. The closed-form equation of the PDF of $\hat{r}$ is hard to obtain. Alternatively, we obtain the approximated form of the PDF by using the PDF fitting tool in MATALAB. By simulation results, we observe that the PDF of $\hat{r}$ fits closely to the Rayleigh distribution:

$$f_{\hat{r}}(\hat{r}) \approx \frac{\hat{r}}{b^2}e^{\frac{-\hat{r}^2}{2b^2}}, \tag{23}$$

where the coefficient $b = 60.7994$ in the fitted PDF, when $m_0 = 10$, $m_{\max} = 100$. Then, we can derive the PDF of θ from the equation $\hat{r} = h\tan(\theta)$ as follows:

$$\begin{aligned} f_{\theta}(\theta) &= \sum f_{\hat{r}}(h\tan\theta)\left|\frac{d\hat{r}}{d\theta}\right| \\ &= \sum f_{\hat{r}}(h\tan\theta)\left|\frac{h^2\tan^2\theta + h^2}{h}\right| \\ &= \frac{h^2\tan\theta}{b^2}e^{-\frac{h^2\tan^2\theta}{2b^2}}\sec^2\theta,\ \left[0 < \theta < \tan^{-1}\left(\frac{2m_{\max}}{h}\right)\right] \end{aligned} \tag{24}$$

The closed-form equations of the PDF of $\hat{\phi}$, $\hat{r}$, θ are simulated in Fig. 8, which are compared with Monte-Carlo simulations. In Fig. 8(b), it is observed that the analytical PDF of $\hat{r}$ based on Rayleigh distribution (red solid line) matches closely with the exact distribution (blue histogram).

B. Expectation of the Channel Gain

The expectation of channel gains can be calculated by the new PDF of random variables. By the similar analysis to the stand-alone scenario, we can obtain the expectation of the channel gain in case of both the ground transmitter with z-axis dipole antenna and the ground transmitter with y-axis dipole antenna, as follows:

$$\begin{aligned} &\mathbb{E}\{|g_{i,i}|^2\}_{\mathrm{z}} \\ &\approx \frac{-3\pi^2k_1e^{-(3k_2)/8}}{512b^2k_2}\left(\sqrt{6\pi k_2}\mathrm{erfi}\left(\frac{\sqrt{k_2}(4\theta^2+3)}{2\sqrt{6}}\right)\right. \\ &\left.-4e^{\frac{1}{24}k_2(4\theta^2+3)^2}\right)\Big|_0^{\tan^{-1}\left(\frac{2m}{h}\right)} = \zeta_{\mathrm{z}}, \end{aligned} \tag{25}$$

$$\begin{aligned} &\mathbb{E}\{|g_{i,i}|^2\}_{\mathrm{y}} \\ &\approx \left(\frac{-3k_1e^{-(3k_2)/8}}{64\pi^2b^2k_2}\right)\left(\frac{5\pi^2}{3} - \frac{\pi^4}{4}\right)\left(\sqrt{6\pi k_2}\right. \\ &\times\ \left.\mathrm{erfi}\left(\frac{\sqrt{k_2}(4\theta^2+3)}{2\sqrt{6}}\right) - 4e^{\frac{1}{24}k_2(4\theta^2+3)^2}\right)\Big|_0^{\tan^{-1}\left(\frac{2m_{\max}}{h}\right)} \\ &+ \left(\frac{k_1e^{-(3k_2)/8}}{4b^2\sqrt{k_2}}\right) \\ &\left(\sqrt{\frac{3\pi}{2}}\mathrm{erfi}\left(\frac{\sqrt{k_2}(4\theta^2+3)}{2\sqrt{6}}\right)\right)\Big|_0^{\tan^{-1}\left(\frac{2m_{\max}}{h}\right)} \\ &= \zeta_{\mathrm{y}}, \end{aligned} \tag{26}$$

where erfi() is the imaginary error function. For the proofs of (25) and (26), see Appendix.

The accuracy of the approximations (25) and (26) are shown in Fig. 9. We observe a similar behavior when compared with the stand-alone scenario in Fig. 6. The closed-form equations are close to the exact values and the approximation accuracy improves as h grows.

In above analysis, we assume onmi-directional Rx antenna, $G_i^{\mathrm{Rx}} = 1$. However, we can also consider the case that IoT

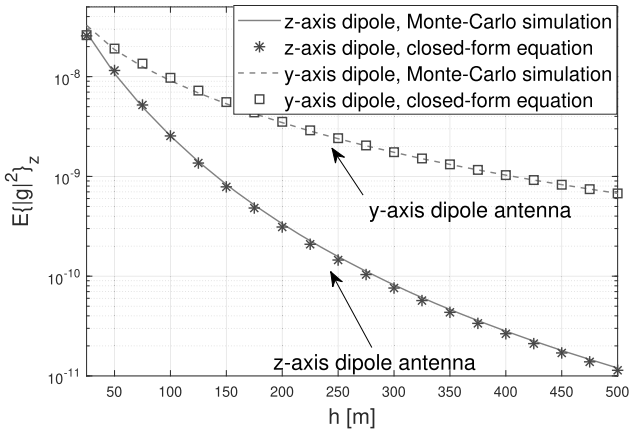

Fig. 9. Expectation of the channel gain versus height (h) with different dipole antenna placement on multiple Tx/Rx pairs scenario in (25), (26). $m_0 = 10$, $m_{\max} = 100$.

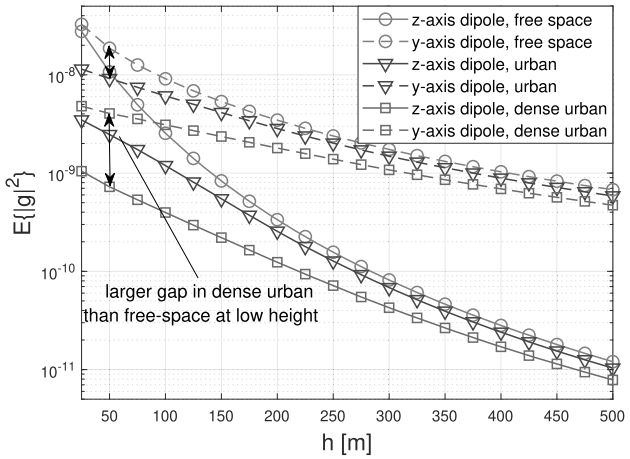

Fig. 10. Expectation of the channel gain versus height (h) with different pathloss models.

receiver equips cross-dipole antenna as well. To achieve the receiver antenna gain, we can adopt our findings from the cross-dipole antenna transmitter setting in a similar way. The ground IoT receiver utilizes the z-axis dipole, while the aerial IoT receiver selects the y-axis dipole antenna by considering the directivity of each antenna configuration. In those cases, the receiver utilizes the same orientation dipole antenna with transmitter dipole antenna (e.g., z-axis dipole antenna and y-axis dipole antenna in both Tx and Rx). Then, the expectation of channel gains of the same orientation dipole antennas can be expressed as follows:

$$\mathbb{E}\{|g_{i,i}|^2\}_{\mathrm{z,z}} = k_1 \mathbb{E}\left\{\frac{(F_{\mathrm{z}})^4}{R^2}\right\}, \tag{27}$$

$$\mathbb{E}\{|g_{i,i}|^2\}_{\mathrm{y,y}} = k_1 \mathbb{E}\left\{\frac{(F_{\mathrm{y}})^4}{R^2}\right\}. \tag{28}$$

We show the expected gain from the cross-dipole receiver antennas by numerical simulation in Fig. 14.

C. Effect of LoS / NLoS Probability

In the previous section, we considered free-space pathloss model to derive the close-form equations about the expectation of the channel gain. In this section, we apply the mixture pathloss model in (5) to observe the effect of LoS probability. The expectation of the channel gain including the effect of LoS probability can be expressed as follows for the ground transmitter with z-axis dipole antenna:

$$\begin{aligned}\mathbb{E}\{|g_{i,i}|^2\}_{\mathrm{z}} &= \mathbb{E}\{PF_{\mathrm{z}}^2/(\beta_{\mathrm{avg}})\alpha^2\} \\ &= \frac{k_1}{\eta_{\mathrm{NLoS}}}\mathbb{E}\left\{\frac{(F_{\mathrm{z}})^2}{R^2} \right. \\ &\quad \left. \times \left(\frac{1 + a_1 \exp(-a_2[90 - \frac{180\theta}{\pi} - a_1])}{\frac{\eta_{\mathrm{LoS}}}{\eta_{\mathrm{NLoS}}} + a_1 \exp(-a_2[90 - \frac{180\theta}{\pi} - a_1])}\right)\right\}\end{aligned} \tag{29}$$

while for the ground transmitter with y-axis dipole antenna, the expectation of teh channel gain is calculated as:

$$\begin{aligned}\mathbb{E}\{|g_{i,i}|^2\}_{\mathrm{y}} &= \frac{k_1}{\eta_{\mathrm{NLoS}}}\mathbb{E}\left\{\frac{(F_{\mathrm{y}})^2}{R^2} \right. \\ &\quad \left. \times \left(\frac{1 + a_1 \exp(-a_2[90 - \frac{180\theta}{\pi} - a_1])}{\frac{\eta_{\mathrm{LoS}}}{\eta_{\mathrm{NLoS}}} + a_1 \exp(-a_2[90 - \frac{180\theta}{\pi} - a_1])}\right)\right\}.\end{aligned} \tag{30}$$

Fig. 10 shows that LoS probability in the pathloss model has positive effect on the reducing interference by the different dipole antenna settings at the low height range. It is observed that the power level gap between z-axis and y-axis dipole antennas is larger at the low height in the dense urban model compared with free-space model, which would reduce interference from z-axis dipole antenna transmitters.

D. Proposed Scheme

We propose an antenna selection strategy where the ground transmitters which are connected with the ground receivers utilize the z-axis dipole antenna, and the ground transmitters which are connected with the aerial receivers utilize the y-axis dipole antenna. In practice, transmitters need to decode messages or receive preambles from receivers in order to know whether the type of receiver is ground or aerial. One feasible way to decide the antenna is by measuring the received signal power of the preambles. In particular, the received signal power from the ground receiver will be higher by selecting the z-axis dipole antenna, while the received signals power from the aerial receiver will be higher by selecting y-axis dipole antenna.

Let $\mathcal{G} = \{F_{\mathrm{z}}^2, F_{\mathrm{y}}^2\}$ be the candidate antenna selection, where $F_{\mathrm{z}}^2, F_{\mathrm{y}}^2$ are the z-axis and the y-axis dipole antenna gains from (11), (12), respectfully. Since we consider cross-dipole setting, with either of the z-axis dipole antenna and the y-axis dipole antenna, the cardinality $|\mathcal{G}|$ is 2. Then, the antenna selection decision is made by the highest received preamble signal power

TABLE I
SIMULATION SETTINGS

Parameter	Value
Minimum radius of circle in ground plane (m_0)	10 m
Maximum radius of circle in ground plane ($m_{\max}$)	100 m
The number of Tx/Rx pairs (K)	5, 10
Transmit power (P)	23 dBm
Carrier frequency (f_0)	800 MHz
Bandwidth (B)	200 kHz
Additive noise power	$-174 + 10\log_{10}(B)$ dBm

as:

$$\{G_i^{\mathrm{Tx}}\}^\star = \arg\max_{\forall G_i^{\mathrm{Tx}} \in \mathcal{G}} PG_i^{\mathrm{Tx}}/(\beta_{i,i})\alpha_{i,i}^2\sigma_s^2, \tag{31}$$

where σ_s^2 is the signal power of the preamble. We verify in Section V-D that this antenna selection approach obtains a very similar performance when compared with the case that the transmitters perfectly know whether the receiver is an aerial or ground receiver.

The ergodic achievable rate of the aerial receiver (i_{th} receiver) can be expressed from (7) as

$$\begin{aligned} S_i &\approx \log_2\left(1 + \frac{\mathbb{E}\{|g_{i,i}|^2\}}{\sum_{j\neq i}\mathbb{E}\{|g_{i,j}|^2\}}\right) \\ &= \log_2\left(1 + \frac{\zeta_{\mathrm{y}}}{(K_{\mathrm{grd}})\zeta_{\mathrm{z}} + (K_{\mathrm{arl}}-1)\zeta_{\mathrm{y}}}\right), \end{aligned} \tag{32}$$

where ζ_{z}, ζ_{y} come from (25) and (26), and K_{grd}, K_{arl} are the number of the grounds transmitters which are connected with the ground receiver and the aerial receiver respectively; $K_{\mathrm{grd}} + K_{\mathrm{arl}} = K$.

V. NUMERICAL RESULTS

In this section, we present simulation results for the performance of the ergodic achievable rate and the sum rate with the proposed schemes. The simulation settings are listed in Table I. We assume that transmitters perfectly know the type of receivers (ground or aerial devices).

A. Ergodic Achievable Rate With Single Aerial Receiver

In Fig. 11, we show the ergodic achievable rate, and desired and interference signal power of the aerial receiver on the scenario in Section III-B. In the scenario, the single aerial receiver is fixed at $(0, 0, h)$ m. In Fig. 11(a), the closed-form equation of z-axis dipole antenna (the red dashed line) comes from (18), and the closed-form equation of y-axis dipole antenna (the blue dashed line) comes from (19). The Monte-Carlo results are directly simulated by the exact ergodic achievable rate in (6). Thus, the gap between closed-form and Monte-Carlo results comes from the approximation procedure in (7). It is observed that the rate gradually increases as the height of the aerial receiver grows in y-axis dipole setting from the ground transmitter (blue curve), while the rate is static in z-axis dipole setting from the ground transmitter (red curve).

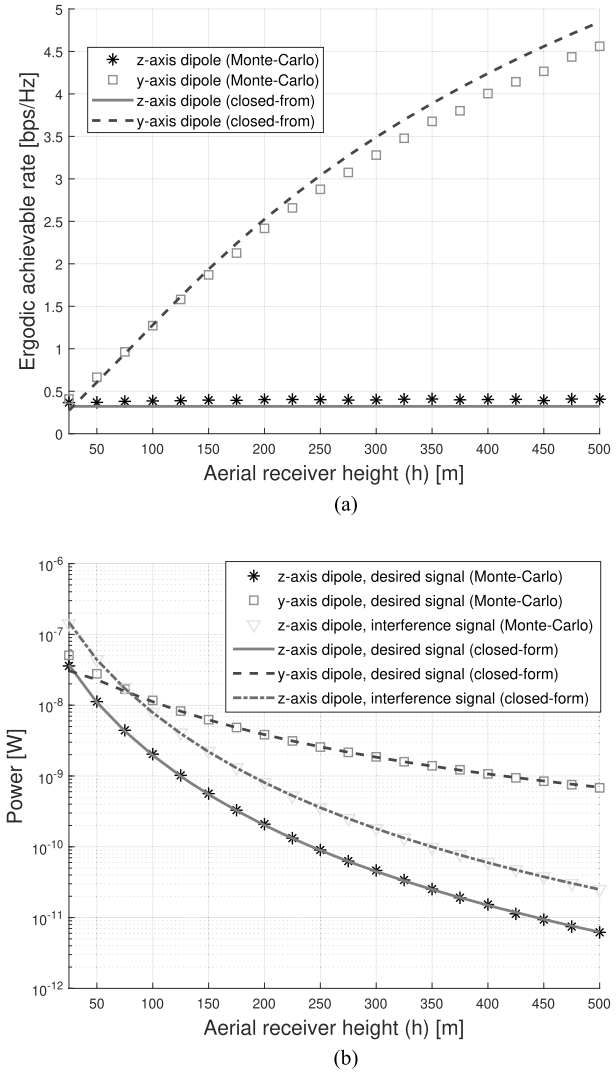

Fig. 11. Ergodic achievable rate and signal power versus the height of the aerial receiver on the scenario in Section III-B with $K = 5$. (a) Ergodic achievable rate. (b) Desired and interference signal power.

The simulation result in Fig. 11(b) shows the consistency with Fig. 11(a) that the gap between desired signal power of y-axis dipole (blue curve) and interference signal power (green curve) keeps increasing, while the gap between desired signal power of z-axis dipole (red curve) and interference signal power (green curve) is constant. Note that we include only the result of interference signal power of z-axis dipole antenna setting, since both the interference signal power of z-axis dipole and y-axis dipole is the same. From the simulation result, we conclude that the performance can be improved by the different antenna radiation pattern depending on the type (ground / aerial) of the receiver. In addition, we show that as the height of the aerial receiver increases, the performance becomes better.

B. Ergodic Achievable Rate of Aerial Receiver With Multiple Tx/Rx Pairs

The ergodic achievable rate of the scenario in Section IV is shown in Fig. 12. In the scenario, all the ground / aerial devices

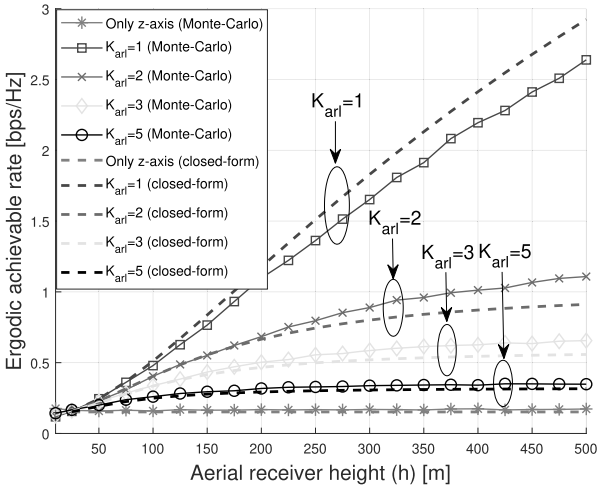

Fig. 12. Ergodic achievable rate versus the height of the aerial receivers on the scenario in Section IV with the different number of aerial receivers (K_{arl}), $K = 10$.

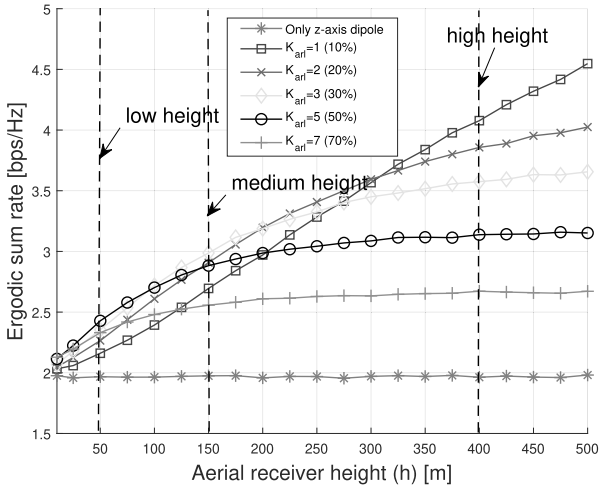

Fig. 13. Ergodic sum rate versusthe height of the aerial receivers on the scenario in Section IV with the different number of aerial receivers (K_{arl}), $K = 10$.

are randomly located at the given space. The transmitters which are connected with the ground receiver utilize z-axis dipole antenna, and the transmitters which are connected with the aerial receiver utilize y-axis dipole antenna. The number of Tx/Rx pairs (K) is 10. The simulation results of closed-form equation come from (32) with the different number of aerial receivers (K_{arl}). We observe that the performance of the achievable rate increases as the height of the aerial receiver increases, while the performance decreases as the number of the aerial receivers increases. It means that as the number of aerial receivers increases, the number of transmitters which utilize y-axis dipole antenna proportionally increases. Then, the power of interference signal toward individual aerial receivers also increases, which degrades the performance. As a reference, we include the simulation results that all transmitters utilize z-axis dipole antenna (red curve), which achieves worse performance with the flat curve.

C. Ergodic Sum Rate of Aerial Receivers With Multiple Tx/Rx Pairs

In Fig. 13, we depict the ergodic sum rate on scenario in Section IV by Monte-Carlo simulations. The number of Tx/Rx pairs is 10 ($K = 10$). the ergodic sum rate is given by $S_{\mathrm{sum}} = \sum_{i=1}^{K} S_i$. In this simulation, we fix the number of Tx/Rx pairs with an increasing number of aerial receivers (K_{arl}). For example, $K_{\mathrm{arl}} = 1$ means that 10% of the overall network are the aerial receivers, while $K_{\mathrm{arl}} = 5$ means that 50% of the network are the aerial receivers. It is observed that depending on the height of aerial receivers, the best ratio between the number of ground and aerial receivers varies. In the case of the low height ($h = 50$ m), 50% of the aerial receivers ($K_{\mathrm{arl}} = 5$) in the network achieves the best rate (black circle line) and the 10% of the aerial receivers ($K_{\mathrm{arl}} = 1$) in the network achieves the worst rate (blue square line). On the other hand, in case of the medium height ($h = 150$ m), 30% of the aerial receivers in the network achieves the best rate (cyan diamond line) and 70% of the aerial receivers in the network achieves the worst rate

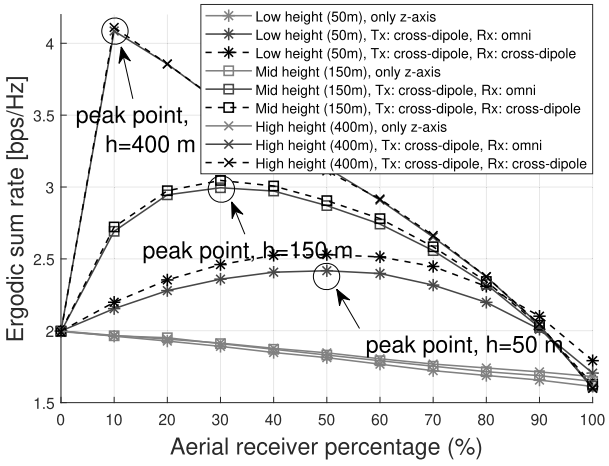

Fig. 14. Ergodic sum rate versus the percentage of the aerial receivers in the network with the different height of the aerial receivers, $K = 10$.

(purple plus line). Furthermore, in the case of the high height ($h = 400$ m), 10% of the aerial receivers in the network achieves the best rate (blue square line) and 70% of the aerial receivers in the network achieves the worst rate (purple plus line). Note that the y-axis dipole antenna to the aerial receiver improves the achievable rate of not only the aerial receivers but also the ground receivers, which reduces the interference in both case.

The ergodic sum rate versus the percentage of the aerial receivers in the network with different height is shown in Fig. 14. We can observe that the point of the peak rate on the percentage of the aerial receivers is different depending on the height. The 50%/30%/10% of the aerial receivers is the peak in low/medium/high height of the aerial receivers. Note that this observation coincides with the result discussed in Fig. 13. We conclude that the best ratio of the ground/aerial receivers in the network is changed by the height of the aerial receivers. In low height, 50% aerial nodes can be the best, but the single aerial receivers can be the best in the high height of the aerial receivers. Also, we compare the proposed cross-dipole antenna

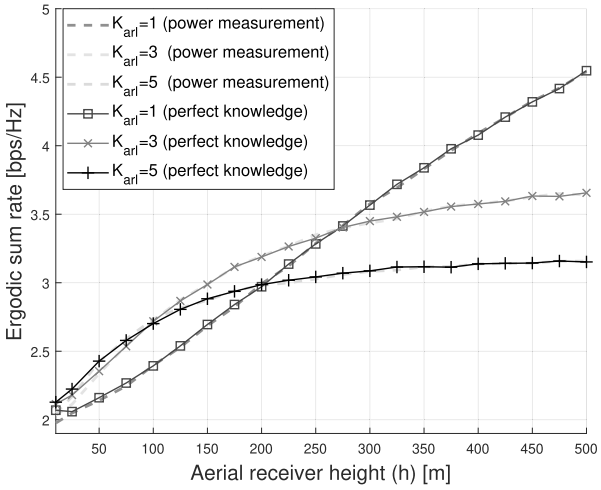

Fig. 15. Ergodic sum rate versus the height of aerial receivers with antenna selections based on perfect knowledge and power measurement, $K = 10$.

scheme (blue curves) with the scheme that transmitters use only z-axis dipole antenna (red curves). We observe that our proposed scheme achieves better performance in all heights.

In Fig. 14, we also compare the performance difference between omni-directional (blue curves) and cross-dipole (black curves) receiver antenna model. Note that in general, we assume an omni-directional receiver antenna in this paper in order to observe the effect of different dipole antenna pattern in the transmitter side. Just for Fig. 14, we also adopt a similar antenna selection approach for cross-dipole antenna receiver, using z-axis dipole antenna for ground receivers and y-axis dipole antenna for aerial receivers. We observe the additional antenna gain from the directivity of receiver antenna especially in low height.

D. Antenna Selection With Received Power Measurements

In previous simulation results, we assume that the transmitters know the type of receivers (i.e., aerial or ground), and choose z-axis or y-axis dipole antenna directly. In this section, we apply the strategy in (31) that selects the antenna by measuring the signal power. In Fig. 15, we compare the ergodic sum rate of antenna selection strategies based on perfect knowledge and measurement. It is observed that the performance between two strategies is close to each other, which means that the performance loss is negligible for the antenna selection based on signal power, when compared with the results for perfectly known receiver

E. Performance With Mixture LoS/NLoS Pathloss Model

Fig. 16 shows the ergodic sum rate with the mixture LoS/NLoS pathloss model in (5) for different aerial receiver heights. The ergodic sum rate is calculated based on (29), (30). It is observed that the performance is improved at the low height case in both urban and dense urban environments compared with the result from the free-space pathloss model (Fig. 14). The observation is coherent with the result in Fig. 10, where the channel gain from z-axis dipole antenna is significantly reduced at the low height.

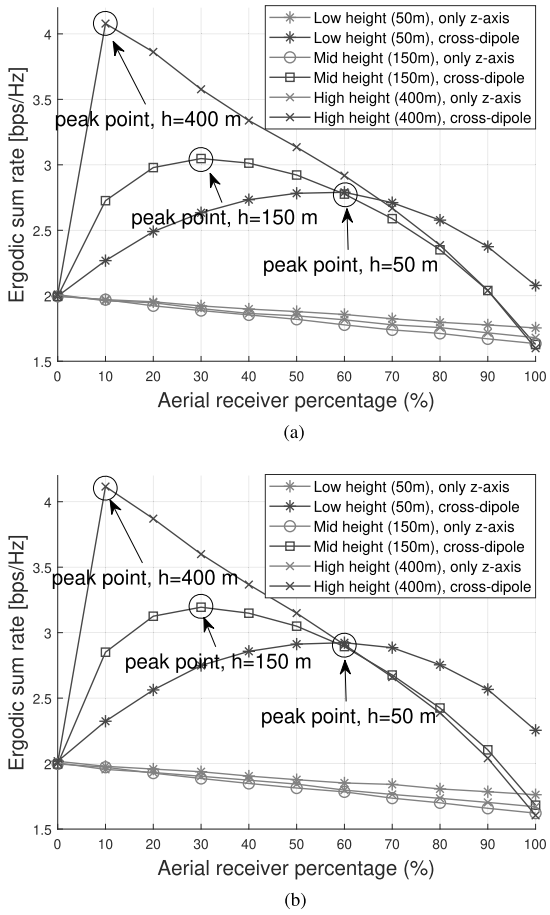

Fig. 16. Ergodic sum rate with pathloss models based on LoS/NLoS probability, $K = 10$. (a) Urban. (b) Dense urban.

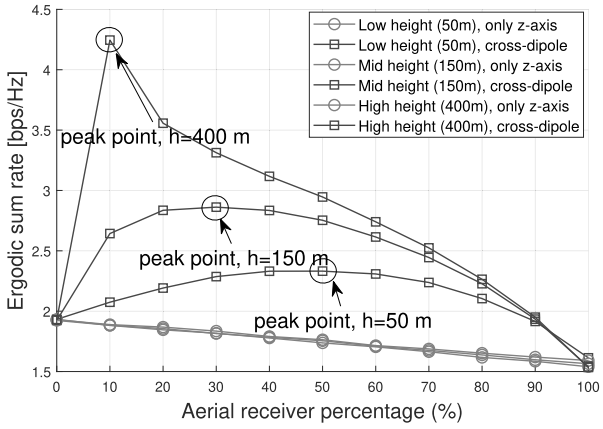

Fig. 17. Ergodic sum rate versus the percentage of the aerial receivers in the network by Rician fading channel in (3), where K-factor = 10 dB.

F. Performance With Rician Fading Channel Model

In Fig. 17, we show the performance in Rician fading channel model in (3) by the ergodic sum rate. We observe that a tendency for the ergodic sum rate is similar to Rayleigh fading channel

model in (2). Note that since the expectation value of the small scale fading coefficient is the same for both Rayleigh and Rician fading model, the analytical approximation result of ergodic achievable rate is the same; $\mathbb{E}\{\alpha^2\} = \mathbb{E}\{\frac{\kappa}{\kappa+1} + \frac{1}{\kappa+1}\alpha^2\} = 1$.

VI. Conclusion

In this paper, we propose and analyze an interference mitigation scheme that utilizes the diversity of the radiation pattern in an uncoordinated aerial/ground IoT network with low-complexity wireless radios. We propose a cross-dipole antenna setting at the transmitter, which utilizes either the z-axis dipole antenna or the y-axis dipole antenna depending on the type of the receivers. We analyze the 3D topology channel model considering the 3D radiation patterns of the dipole antennas and the locations of the IoT devices, and we analytically show that the y-axis dipole antenna achieves better performance for aerial receivers than the z-axis dipole antenna. By simulation results, we observe that the cross-dipole antenna scheme outperforms the scheme that only uses the z-dipole antenna, and we can improve the performance by increasing the height of the aerial receivers. In addition, depending on the height of the aerial receivers (low/medium/high), the best ratio of the ground receiver to aerial receiver varies, which is studied for various propagation scenarios. In this paper, we focus on the effect of the cross-dipole antenna configuration on the IoT transmitter. Therefore, we assume that the receiver is equipped with an onmi-directional antenna pattern. An extension of this scenario includes the IoT receiver being also equipped with cross-dipole antennas. It is observed that we obtain additional gain especially on low altitude range from the receiver antenna pattern by the proposed scheme.

Appendix
Proof of Equations (25), (26)

We may rewrite (13) after some manipulation as:

$$\begin{aligned}
\mathbb{E}\{|g_{i,i}|^2\}_{\mathrm{z}} &= k_1 \mathbb{E}\left\{\frac{(F_{\mathrm{z}})^2}{R^2}\right\} \\
&= k_1 \mathbb{E}\left\{\left(\frac{\cos\left(\frac{\pi}{2}\cos\theta\right)}{\sin\theta}\right)^2 \frac{\cos^2\theta}{h^2}\right\} \\
&= k_1 \int \left(\frac{\cos\left(\frac{\pi}{2}\cos\theta\right)}{h\sin\theta}\right)^2 \cos^2\theta \; f_\theta(\theta)\mathrm{d}\theta \\
&= \frac{k_1}{b^2}\int_0^{\tan^{-1}\left(\frac{2m_{\max}}{h}\right)} \left(\frac{\cos\left(\frac{\pi}{2}\cos\theta\right)}{\sin\theta}\right)^2 \\
&\quad \times \left(\tan\theta e^{k_2\tan^2\theta}\right)\mathrm{d}\theta, \qquad (33)
\end{aligned}$$

where F_{z}, $f_\theta(\theta)$ come from (11), (24), and $k_2 = \frac{-h^2}{2b^2}$. If the height (h) goes to infinity, the interval of the integral with respect to θ goes to 0 ($\tan^{-1}\left(\frac{2m_{\max}}{h}\right) \to 0$, as $h \to \infty$).

Then, we can apply Taylor series approximation at $\theta = 0$ as follows:

$$\begin{aligned}
&\mathbb{E}\{|g_{i,i}|^2\}_{\mathrm{z}} \\
&\approx \frac{k_1}{b^2}\int_0^{\tan^{-1}\left(\frac{2m_{\max}}{h}\right)} \left(\frac{\pi^2\theta^3}{16}\right)\left(e^{k_2(\theta^2+\frac{2}{3}\theta^4)}\right)\mathrm{d}\theta, \qquad (34)
\end{aligned}$$

where $\frac{\pi^2\theta^3}{16}$ is the first term of Taylor series of $(\cos(\frac{\pi}{2}\cos\theta)/\sin\theta)^2(\tan\theta)$, and $\theta^2 + \frac{2}{3}\theta^4$ includes the first and the second terms of the Taylor series of $\tan^2\theta$. By solving (34), we can obtain (25).

Similarly, the proof of equation (26) is obtained by starting from (16) as follows:

$$\begin{aligned}
&\mathbb{E}\{|g_{i,i}|^2\}_{\mathrm{y}} \\
&= k_1 \mathbb{E}\left\{\frac{(F_{\mathrm{y}})^2}{R^2}\right\} \\
&= k_1 \mathbb{E}\left\{\left(\frac{\cos\left(\frac{\pi}{2}\cos(\cos^{-1}(\sin(\theta)\sin(\hat{\phi})))\right)}{h\sin\left(\cos^{-1}(\sin(\theta)\sin(\hat{\phi}))\right)}\right)^2 \frac{\cos^2\theta}{h^2}\right\} \\
&= k_1 \int\int \left(\frac{\cos\left(\frac{\pi}{2}\cos(\cos^{-1}(\sin(\theta)\sin(\hat{\phi})))\right)}{h\sin\left(\cos^{-1}(\sin(\theta)\sin(\hat{\phi}))\right)}\right)^2 \\
&\quad \times \cos^2\theta \; f_\theta(\theta) f_{\hat{\phi}}(\hat{\phi})\mathrm{d}\theta\mathrm{d}\hat{\phi} \\
&= \frac{k_1}{2\pi^2 b^2}\int_0^{2\pi}\int_0^{\tan^{-1}\left(\frac{2m_{\max}}{h}\right)} \\
&\quad \times \left(\frac{\cos\left(\frac{\pi}{2}\cos(\cos^{-1}(\sin(\theta)\sin(\hat{\phi})))\right)}{\sin\left(\cos^{-1}(\sin(\theta)\sin(\hat{\phi}))\right)}\right)^2 \\
&\quad \times \left(\tan\theta e^{k_2\tan^2\theta}\right)\left(2\pi - \hat{\phi}\right)\mathrm{d}\theta\mathrm{d}\hat{\phi}, \qquad (35)
\end{aligned}$$

where F_{y}, $f_{\hat{\phi}}(\hat{\phi})$, and $f_\theta(\theta)$ come from (12), (22), (24), respectively. After applying Taylor series approximation, (35) can be rewritten as

$$\begin{aligned}
&\mathbb{E}\{|g_{i,i}|^2\}_{\mathrm{y}} \\
&\approx \frac{k_1}{2\pi^2 b^2}\int_0^{2\pi}\int_0^{\tan^{-1}\left(\frac{2m_{\max}}{h}\right)} \\
&\quad \times \left(\theta + \left(\sin^2(\hat{\phi}) - \frac{\pi^2\sin^2(\hat{\phi})}{4} + \frac{1}{3}\right)\theta^3\right) \\
&\quad \times \left(e^{k_2(\theta^2+\frac{2}{3}\theta^4)}\right)\left(2\pi - \hat{\phi}\right)\mathrm{d}\theta\mathrm{d}\hat{\phi} \\
&= \frac{k_1}{2\pi^2 b^2}\int_0^{\tan^{-1}\left(\frac{2m_{\max}}{h}\right)} \left(2\pi^2\theta + \left(\frac{5\pi^2}{3} - \frac{\pi^4}{4}\right)\theta^3\right) \\
&\quad \times \left(e^{k_2(\theta^2+\frac{2}{3}\theta^4)}\right)\mathrm{d}\theta, \qquad (36)
\end{aligned}$$

where $(\theta + (\sin^2(\hat{\phi}) - \frac{\pi^2 \sin^2(\hat{\phi})}{4} + \frac{1}{3})\theta^3)$ includes the first and the second terms of the Taylor series at $\theta = 0$ with fixed $\hat{\phi}$. By solving (36), we can obtain (26).

REFERENCES

[1] S. J. Maeng, M. A. Deshmukh, I. Guvenc, and A. Bhuyan, "Interference mitigation scheme in 3D topology IoT network with antenna radiation pattern," in *Proc. IEEE Veh. Technol. Conf.*, Honolulu, HI, USA, Sep. 2019, pp. 1–6.

[2] A. Gupta and R. K. Jha, "A survey of 5G network: Architecture and emerging technologies," *IEEE Access*, vol. 3, pp. 1206–1232, Jul. 2015.

[3] A. Whitmore, A. Agarwal, and L. Da Xu, "The Internet of Things—A survey of topics and trends," *Inf. Syst. Front.*, vol. 17, no. 2, pp. 261–274, Apr. 2015.

[4] A. Ijaz *et al.*, "Enabling massive IoT in 5G and beyond systems: Phy radio frame design considerations," *IEEE Access*, vol. 4, pp. 3322–3339, Jun. 2016.

[5] A. Al-Fuqaha, M. Guizani, M. Mohammadi, M. Aledhari, and M. Ayyash, "Internet of Things: A. survey on enabling technologies, protocols, and applications," *IEEE Commun. Surv. Tut.*, vol. 17, no. 4, pp. 2347–2376, Jun. 2015.

[6] S. Popli, R. K. Jha, and S. Jain, "A survey on energy efficient narrowband Internet of Things (NBIoT): Architecture, application and challenges," *IEEE Access*, vol. 7, pp. 16 739–16 776, Nov. 2018.

[7] A. Rico-Alvarino *et al.*, "An overview of 3GPP enhancements on machine to machine communications," *IEEE Commun. Mag.*, vol. 54, no. 6, pp. 14–21, Jun. 2016.

[8] R. S. Sinha, Y. Wei, and S.-H. Hwang, "A survey on LPWA technology: LoRa and NB-IoT," *ICT Express*, vol. 3, no. 1, pp. 14–21, Mar. 2017.

[9] Y. Zeng, J. Lyu, and R. Zhang, "Cellular-connected UAV: Potential, challenges, and promising technologies," *IEEE Wireless Commun.*, vol. 26, no. 1, pp. 120–127, Sep. 2018.

[10] Z. Xiao, P. Xia, and X.-G. Xia, "Enabling UAV cellular with millimeter-wave communication: Potentials and approaches," *IEEE Commun. Mag.*, vol. 54, no. 5, pp. 66–73, May 2016.

[11] N. H. Motlagh, M. Bagaa, and T. Taleb, "UAV-based IoT platform: A. crowd surveillance use case," *IEEE Commun. Mag.*, vol. 55, no. 2, pp. 128–134, Feb. 2017.

[12] T. Wei and X. Zhang, "Gyro in the air: Tracking 3D orientation of batteryless Internet-of-Things," in *Proc. Int. Conf. Mobile Comput. Netw.*, 2016, pp. 55–68.

[13] B. S. Ciftler, A. Kadri, and I. Güvenç, "IoT localization for bistatic passive UHF RFID systems with 3-D radiation pattern," *IEEE Internet Things J.*, vol. 4, no. 4, pp. 905–916, Apr. 2017.

[14] A. Bujari, M. Furini, F. Mandreoli, R. Martoglia, M. Montangero, and D. Ronzani, "Standards, security and business models: Key challenges for the IoT scenario," *Mobile Netw. Appl.*, vol. 23, no. 1, pp. 147–154, Feb. 2018.

[15] Y. Teng, M. Liu, F. R. Yu, V. C. Leung, M. Song, and Y. Zhang, "Resource allocation for ultra-dense networks: A. survey, some research issues and challenges," *IEEE Commun. Surv. Tut.*, vol. 21, no. 3, pp. 2134–2168, Aug. 2018.

[16] D. Zucchetto and A. Zanella, "Uncoordinated access schemes for the IoT: Approaches, regulations, and performance," *IEEE Commun. Mag.*, vol. 55, no. 9, pp. 48–54, Sep. 2017.

[17] A. Kammoun *et al.*, "3D massive MIMO systems: Modeling and performance analysis," *IEEE Trans. Wireless Commun.*, vol. 14, no. 12, pp. 6926–6939, Dec. 2015.

[18] M. Baianifar, S. Khavari, S. M. Razavizadeh, and T. Svensson, "Impact of user height on the coverage of 3D beamforming-enabled massive MIMO systems," in *Proc. Int. Symp. Pers., Indoor, Mobile Radio Commun.*, 2017, pp. 1–5.

[19] Y. Li, X. Ji, D. Liang, and Y. Li, "Dynamic beamforming for three-dimensional MIMO technique in LTE-advanced networks," *Int. J. Antennas Propag.*, vol. 2013, 2013.

[20] M. Rebato, J. Park, P. Popovski, E. De Carvalho, and M. Zorzi, "Stochastic geometric coverage analysis in mmWave cellular networks with realistic channel and antenna radiation models," *IEEE Trans. Commun.*, vol. 67, no. 5, pp. 3736–3752, Jan. 2019.

[21] 3GPP, "Study on channel model for frequencies from 0.5 to 100 GHz," Version 14.2.0, Tech. Rep. 38.901, Sep. 2017.

[22] G. Geraci, A. Garcia-Rodriguez, L. G. Giordano, D. López-Pérez, and E. Björnson, "Understanding UAV cellular communications: From existing networks to massive MIMO," *IEEE Access*, vol. 6, pp. 67 853–67 865, Nov. 2018.

[23] L. Zhu, J. Zhang, Z. Xiao, X. Cao, D. O. Wu, and X.-G. Xia, "3-D beamforming for flexible coverage in millimeter-wave UAV communications," *IEEE Wireless Commun. Lett.*, vol. 8, no. 3, pp. 837–840, Jun. 2019.

[24] J. Chen, D. Raye, W. Khawaja, P. Sinha, and I. Guvenc, "Impact of 3D UWB antenna radiation pattern on air-to-ground drone connectivity," in *Proc. IEEE Veh. Technol. Conf.*, Sep. 2018, pp. 1–5.

[25] M. Shafi *et al.*, "Polarized MIMO channels in 3-D: Models, measurements and mutual information," *IEEE J. Sel. Areas Commun.*, vol. 24, no. 3, pp. 514–527, Mar. 2006.

[26] M.-T. Dao, V.-A. Nguyen, Y.-T. Im, S.-O. Park, and G. Yoon, "3D polarized channel modeling and performance comparison of MIMO antenna configurations with different polarizations," *IEEE Trans. Antennas Propag.*, vol. 59, no. 7, pp. 2672–2682, May 2011.

[27] FAA, "Remote Identification of Unmanned Aircraft Systems," FAA Notice of Proposed Rule Making (FAA-2019-1100), Dec. 2019.

[28] ITU-R, "Propagation data and prediction methods required for the design of terrestrial broadband radio access systems," *P. Ser., Radiow. Propag.*, Rep. P.1410-5, Feb. 2012.

[29] A. Al-Hourani, S. Kandeepan, and S. Lardner, "Optimal LAP altitude for maximum coverage," *IEEE Wireless Commun. Lett.*, vol. 3, no. 6, pp. 569–572, Jul. 2014.

[30] A. Al-Hourani, S. Kandeepan, and A. Jamalipour, "Modeling air-to-ground path loss for low altitude platforms in urban environments," in *Proc. IEEE Globecom*, Austin, TX, USA, Dec. 2014, pp. 2898–2904.

[31] Q. Zhang, S. Jin, K.-K. Wong, H. Zhu, and M. Matthaiou, "Power scaling of uplink massive MIMO systems with arbitrary-rank channel means," *IEEE J. Sel. Top. Signal Process*, vol. 8, no. 5, pp. 966–981, May 2014.

[32] L. Fan, S. Jin, C.-K. Wen, and H. Zhang, "Uplink achievable rate for massive MIMO systems with low-resolution ADC," *IEEE Commun. Lett.*, vol. 19, no. 12, pp. 2186–2189, Oct. 2015.

[33] C. A. Balanis, *Antenna Theory: Analysis and Design*, John Wiley & Sons, 2016.

[34] P. Chandhar, D. Danev, and E. G. Larsson, "Massive MIMO for communications with drone swarms," *IEEE Trans. Wireless Commun.*, vol. 17, no. 3, pp. 1604–1629, Dec. 2017.

Sung Joon Maeng received the B.S. and M.S. degrees in electrical and electronic engineering from Chung-Ang University, South Korea, in 2015 and 2017, respectively. He is currently working toward the Ph.D. degree in electrical and computer engineering with North Carolina State University. His main research interests include mmWave communication, massive MIMO, and drone-based wireless communication.

Mrugen A. Deshmukh received the B.E. degree in electronics engineering from the University of Pune, India, in 2015 after which he worked as an Engineering Intern with General Electric, Pune, India for three months. In 2018, he completed the M.S. degree in electrical engineering from the University of Virginia. He is currently working toward the Ph.D. degree in electrical and computer engineering with North Carolina State University.

İsmail Güvenç (Fellow, IEEE) received the Ph.D. degree in electrical engineering from the University of South Florida in 2006. He was with the Mitsubishi Electric Research Labs in 2005, with DOCOMO Innovations from 2006 to 2012, and with Florida International University, from 2012 to 2016. From 2016 to 2020, he has been an Associate Professor, and since 2020, he has been a Professor, with the Department of Electrical and Computer Engineering of North Carolina State University. He has authored or coauthored more than 290 conference/journal articles and book chapters, and several standardization contributions. He coauthored or Co-Edited four books and he is an Inventor/Co-Inventor of some 30 U.S. patents. His recent research interests include 5G wireless systems, communications and networking with drones, and heterogeneous wireless networks.

Dr. Güven is a Senior Member with the National Academy of Inventors. He was the recipient of the USF Outstanding Dissertation Award in 2006, the Ralph E. Powe Junior Faculty Enhancement Award in 2014, the NSF CAREER Award in 2015, the FIU College of Engineering Faculty Research Award in 2016, and the NCSU ECE R. Ray Bennett Faculty Fellow Award in 2019. He was an Editor for the IEEE COMMUNICATIONS LETTERS from 2010 to 2015 and the IEEE WIRELESS COMMUNICATIONS LETTERS from 2011 to 2016. He has been serving as an Editor for the IEEE TRANSACTIONS ON WIRELESS COMMUNICATIONS since 2016. He was a Guest Editor for several other journals.

Arupjyoti (Arup) Bhuyan (Senior Member, IEEE) received the Ph.D. degree in engineering and applied sciences from Yale University. He is a Wireless Researcher with Idaho National Laboratory (INL) and the Technical Director with INL Wireless Security Institute. His research interests include secure implementation of future generations of wireless communications with scientific exploration and engineering innovations across the fields of wireless technology, cybersecurity, and computational science. Specific goals are to assure communications among critical infrastructure systems supporting control of the electric grid, emergency response, and nationwide unmanned aerial systems. He has extensive industry experience in wireless communications from his work before he joined INL in October, 2015.

Huaiyu Dai (Fellow, IEEE) received the B.E. and M.S. degrees in electrical engineering from Tsinghua University, Beijing, China, in 1996 and 1998, respectively, and the Ph.D. degree in electrical engineering from Princeton University, Princeton, NJ, in 2002.

He was with Bell Labs, Lucent Technologies, Holmdel, NJ, in 2000, and with AT&T Labs-Research, Middletown, NJ, in 2001. He is currently a Professor of Electrical and Computer Engineering with NC State University, Raleigh, holding the title of University Faculty Scholar. His research interests include general areas of communications, signal processing, networking, and computing. His current research interests include machine learning and artificial intelligence for communications and networking, multilayer and interdependent networks, dynamic spectrum access and sharing, as well as security and privacy issues in the above systems.

He was an Editor of IEEE TRANSACTIONS ON COMMUNICATIONS, IEEE TRANSACTIONS ON SIGNAL PROCESSING, and IEEE TRANSACTIONS ON WIRELESS COMMUNICATIONS. He is currently an Area Editor in charge of wireless communications for IEEE TRANSACTIONS ON COMMUNICATIONS, and a member of the Executive Editorial Committee for IEEE TRANSACTIONS ON WIRELESS COMMUNICATIONS. He was the Co-Recipient of Best Paper Awards at 2010 IEEE International Conference on Mobile Ad-hoc and Sensor Systems (MASS 2010), 2016 IEEE INFOCOM BIGSECURITY Workshop, and 2017 IEEE International Conference on Communications (ICC 2017).